Energy & Environmental Science

COMMUNICATION

View Article Online
View Journal | View Issue

Cite this: *Energy Environ. Sci.*, 2018, **11**, 2016

Received 27th April 2018,
Accepted 13th June 2018

DOI: 10.1039/c8ee01244j

rsc.li/ees

Solar thermal-driven capacitance enhancement of supercapacitors†

Fang Yi,‡[a] Huaying Ren,‡[a] Keren Dai,‡[b] Xiaofeng Wang,[b] Yingzhou Han,[b] Kexin Wang,[a] Ke Li,[c] Baolu Guan,[d] Jie Wang,[e] Miao Tang,[a] Jingyuan Shan,[a] Hao Yang,[a] Mingsheng Zheng,[f] Zheng You,[b] Di Wei *[c] and Zhongfan Liu *[ac]

Solar energy is a renewable and abundant energy source that has myriad potential applications to be tapped. Energy storage devices often present diminishing performance at lower temperatures, and sometimes they even fail during cold weather; therefore, a renewable technology to spur such sluggish performance not only is important for a sustainable future but also may inspire new-concept devices such as ignition sensors. Here, under solar illumination, the capacitance, energy density and power density of supercapacitors are all largely enhanced owing to the photo-thermal effect. The supercapacitors employ three-dimensional hierarchical graphene as the electrodes, and show an absorption of >92.88% over the entire solar spectrum, a response time of <200 s, and a surface temperature change of ~39 °C under 1 solar illumination (1 kW m^{-2}). Under 1 solar illumination, the capacitance of the pseudocapacitor increases by ~1.5 times, and the capacitance of the electric double-layer capacitor increases by ~3.7 times. The mechanism is quantitatively analyzed and discussed. This work provides new insights into the applications of solar energy and offers new design options for the development of energy storage devices.

Broader context

Solar energy is a renewable and abundant energy source that plays an important role to achieve a sustainable future. Solar thermal energy converts solar light into heat and has many applications such as solar desalination and power generation. Supercapacitors are a widely used energy storage device with advantages such as high power density, fast charge/discharge rates and long cycling life. However, like other energy storage devices, supercapacitors often show lower performance at lower temperatures. Here, we use solar thermal energy for elevating the capacitance, energy density and power density of supercapacitors. The supercapacitors are based on three-dimensional hierarchical graphene that has high broadband light absorption and high thermal conductivity. It is found that the pseudocapacitor capacitance increases by ~1.5 times and the electric double-layer capacitor capacitance increases by ~3.7 times under 1 solar illumination. On the basis of the proof-of-concept presented here, solar thermal energy could act as a renewable technology to potentially address the failure problem of energy storage devices during cold weather and may initiate new-concept sensors. This work may inspire new insights for the application of solar energy and the design of energy storage devices.

Introduction

Owing to its abundant resources and important role in reducing greenhouse gas emissions, renewable energy is one of the hottest topics revolving around the world nowadays. Solar energy is a tantalizing renewable energy resource that reaches the earth's surface with a quantity of energy far exceeding human needs.[1] Among the solar energy harvesting technologies that are witnessing rapid development, such as photovoltaics, photocatalysis, and artificial photosynthesis, solar thermal technology that converts sunlight into heat is a promising aspect and has gained intensive attention due to its high conversion efficiency and low lost.[2–7] Up to now, solar thermal conversion has been developed for many applications including solar-steam generation, photo-thermal therapy, and power generation;[8–11] however, it still has a large untapped potential for diverse futuristic applications.

Energy storage devices are an essential part in today's world. Supercapacitors are an important energy storage device with

[a] *Center for Nanochemistry, Beijing Science and Engineering Center for Nanocarbons, Beijing National Laboratory for Molecular Sciences, College of Chemistry and Molecular Engineering, Peking University, Beijing 100871, China. E-mail: zfliu@pku.edu.cn*
[b] *Department of Precision Instrument, Center for Flexible Electronics Technology, Tsinghua University, Beijing 100084, P. R. China*
[c] *Beijing Graphene Institute, Beijing 100095, P. R. China. E-mail: weidi-cnc@pku.edu.cn*
[d] *Key Laboratory of Opto-electronics Technology, Ministry of Education, College of Electronic Science and Technology, Faculty of Information Technology, Beijing University of Technology, Beijing 100022, P. R. China*
[e] *Beijing Institute of Nanoenergy and Nanosystems, Chinese Academy of Sciences, National Center for Nanoscience and Technology, Beijing 100083, China*
[f] *College of Biological and Chemical Engineering, University of Science and Technology Beijing, Beijing 100083, P. R. China*

† Electronic supplementary information (ESI) available. See DOI: 10.1039/c8ee01244j

‡ These authors contributed equally to this work.

the merits of high power density, fast charge/discharge ability, and long cycle life.[12–22] The typical supercapacitors include electric double-layer capacitors that are mainly based on ion adsorption/desorption and pseudocapacitors that are mainly based on fast Faradaic reactions. Supercapacitors have a wide range of applications in areas such as transportation, consumer electronics and sustainable energy systems.[23–28] However, like other energy storage devices, supercapacitors usually provide diminishing power at lower temperatures, and sometimes they even fail during cold weather. In this regard, a renewable and low-cost way to spur the sluggish performance not only can help to address such problems but also may initiate new-concept devices such as ignition, optical or temperature sensors.

Graphene has been regarded as a promising photothermal material due to its intriguing attributes of lightweight property, broadband light absorption, low molar specific heat, high Debye temperature, and high thermal conductivity.[29–33] Specifically, three-dimensional (3D) graphene has a porous structure with increased surface area, which provides sufficient heat exchange contact and leads to high solar thermal conversion efficiency.[34–36] Moreover, the freestanding interconnected hierarchical architecture also makes 3D graphene promising for supercapacitors, which not only prevents the restacking of graphene sheets but also enables easy access and diffusion of various ions and molecules.[37–44] Its other fascinating features such as high electron mobility, lightweight property, excellent chemical stability and flexibility also drive the race for developing new-generation supercapacitors.

Here, supercapacitors based on 3D-hierarchical (3D-h) graphene were found to have greatly elevated capacitance, energy density, and power density under solar illumination due to the photothermal effect. The supercapacitors are structured with two parallel 3D-h graphene electrodes and a solid-state PVA/H_3PO_4 electrolyte. The supercapacitors have an absorption of $>92.88\%$ in the whole solar spectrum, a response time of <200 s, and a surface temperature change (ΔT) of ~ 39 °C when the light illumination intensity is 1 kW m^{-2}. Under 1 solar illumination (1 kW m^{-2}), the capacitance of the pseudo-type supercapacitor increases by 1.5 times, the energy density increases by ~ 1.5 times and the power density increases by ~ 1.6 times. The capacitance of the double-layer-type supercapacitor increases by ~ 3.7 times under 1 solar illumination. The variable parameters contributing to the elevated capacitances of the supercapacitors were analyzed and discussed. The mechanism was further verified by heating the supercapacitors at various temperatures.

Results

As schematically illustrated in Fig. 1a, when the supercapacitor is under solar illumination, solar light is converted into heat, which raises the temperature of the supercapacitor and results in an enhancement of the capacitance. 3D-h graphene is employed as the basic electrodes of the supercapacitor, which has an absorption of $>91\%$ over the full solar spectrum (Fig. 2c). The pseudo-type supercapacitor has two plane parallel electrodes (Fig. 1b), with PEDOT:PSS as the active material and the solid-state PVA/H_3PO_4 compound as the electrolyte. Note that in the following paragraphs, the term "supercapacitor" refers to this pseudo-type supercapacitor unless otherwise mentioned. This kind of structure allows the supercapacitor to have a large solar irradiated

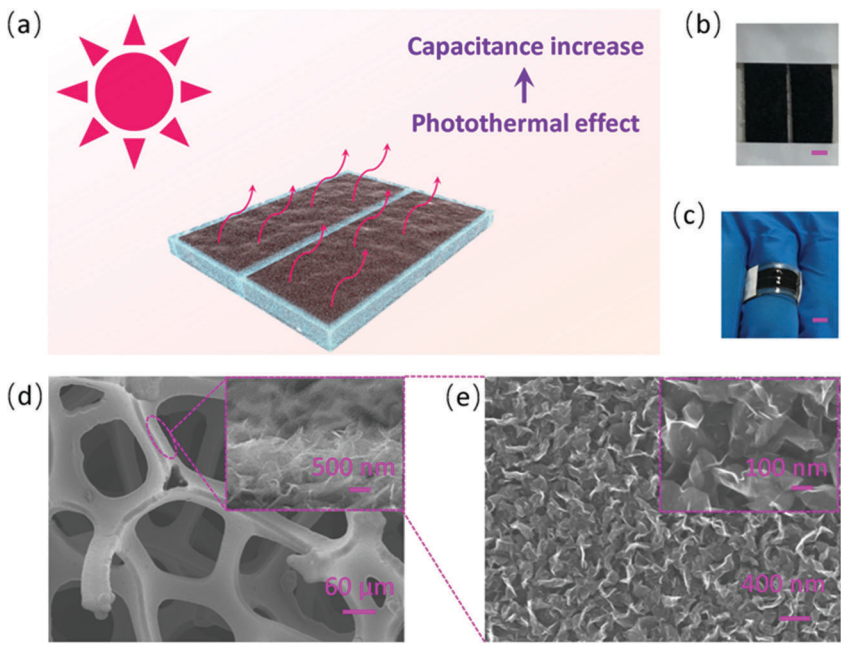

Fig. 1 Schematic illustration of the photothermal effect enhanced capacitance and a typical structure of the supercapacitor. (a) Schematic illustration of the increasing capacitance by the photothermal effect. (b) Photograph of the supercapacitor. Scale bar, 1 mm. (c) Photograph of the supercapacitor worn on a finger. Scale bar, 5 mm. (d) SEM images showing the hollow self-supporting bone structure with densely packed nanoplates of the 3D-h graphene. (e) Enlarged view of the graphene nanoplates on the bone surface.

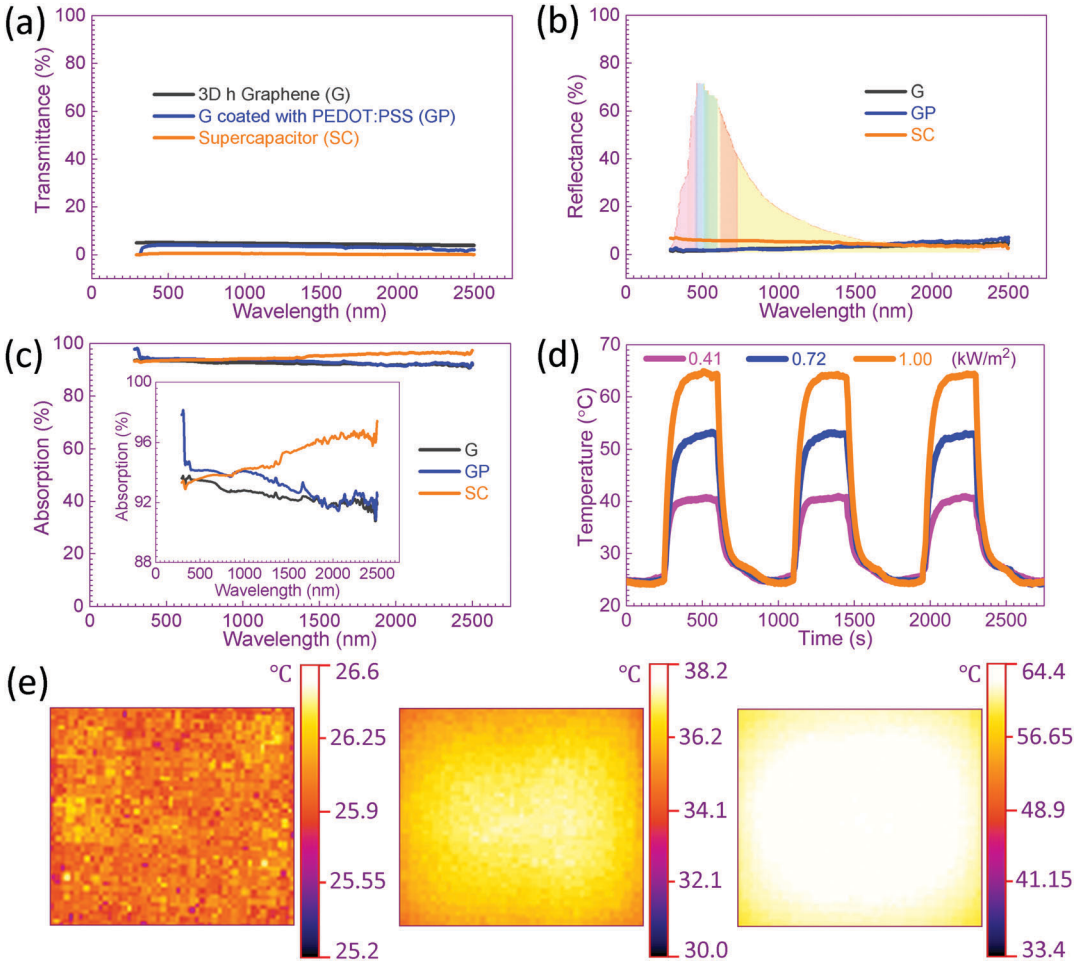

Fig. 2 Light absorption and heat conversion of the supercapacitor. (a–c) The (a) transmittance, (b) reflectance, and (c) absorption of the 3D-h graphene, 3D-h graphene coated with PEDOT:PSS and supercapacitor. (d) The temperature responses of the supercapacitor under solar illumination at power densities of 0.41, 0.72 and 1 kW m^{-2}. (e) Infrared images of the supercapacitor under 1 solar illumination.

area and endows the supercapacitor with robustness and flexibility, which can be worn on the human body (Fig. 1c). Note that the double-layer-type supercapacitors, which have the same device structure only without PEDOT:PSS, are also seen to exhibit a large capacitance enhancement under solar illumination (more details will be discussed later). The 3D-h graphene was grown by a plasma enhanced chemical vapor deposition method using nickel foam as the substrate. The SEM images show that the as-synthesized 3D-h graphene has a hollow self-supporting bone structure with densely packed graphene nanoplates on the bone surface (Fig. 1d and e). The TEM observation shows that the graphene nanoplates contain 6–10 layers (Fig. S1a and b, ESI†), and the Raman spectrum reveals that the 3D-h graphene possesses high crystal quality (Fig. S1c, ESI†). The PEDOT:PSS was coated on the 3D-h graphene by a dip-and-dry method, and has a thickness of 4–8 nm (Fig. S2, ESI†). The detailed fabrication processes of the 3D-h graphene and the supercapacitor can be found in the methods.

The 3D-h graphene plays a key role in the solar thermal conversion process. Firstly, the unique electronic structure of graphene endows it with an optical absorption independent of wavelength,[45,46] and the absorbed light energy is mostly converted to heat.[47] Secondly, the graphene nanoplates that are anchored on the bone surface extend the light-matter interaction length, increase the light collection, and reduce the light reflection,[29] therefore largely improving the absorption of sunlight (Fig. S3, ESI†). As shown in Fig. 2a–c, the 3D-h graphene has a transmittance of $<5.1\%$, a reflectance of $<5.4\%$ and an absorption of $>91\%$ over the full solar spectrum (the solar spectrum on the earth's surface ranges from $\sim$295 to $\sim$2500 nm). After being coated with PEDOT:PSS and filled with the PVA/H_3PO_4 electrolyte, the fabricated supercapacitor exhibits a lower transmittance, a slightly higher reflectance, and a higher absorption ($>92.88\%$ over the entire solar spectrum) compared with the 3D-h graphene (Fig. 2a–c). With such high absorption ability of sunlight, the supercapacitor shows a solar-thermal conversion efficiency η_{st} of $\sim$18.56%. The η_{st} was achieved from the thermal profile as shown in Fig. 2d, through the energy balance function:[6,38,39]

$$\sum m_i C_{p,i} \frac{dT}{dt} = \dot{Q}_{in} - \dot{Q}_{surr,out} \quad (1)$$

where m_i and $C_{p,i}$ are the mass and specific heat capacity of the system components, respectively and $\dot{Q}_{in}$ and $\dot{Q}_{surr,out}$ are the heat input from the material and heat dissipation to the surroundings, respectively. The detailed calculation of η_{st} can be found in Note S1 (ESI†). It can be seen from eqn (1) that for a given device with determined materials, the temperature of the illuminated device can be easily controlled by controlling the power density of the light irradiated on the device, for example, tuning the power of the light source (laser diodes, lamps, *etc.*), adding an optical concentrator or attenuator between the light source and device, and so on. The surface temperature change (ΔT) of the supercapacitor increases from ~15 °C to ~39 °C when the power density of the solar light increases from 0.41 kW m^{-2} to 1 kW m^{-2} (Fig. 2d). The time required to reach the steady-state temperature is within 200 s, and the temperature response has good repeatability. Fig. 2e shows the infrared images of the supercapacitor under 1 solar illumination (1 kW m^{-2}), which visualizes the increasing temperature of the supercapacitor during the irradiation process.

Note that during the solar illumination experiments, the active material PEDOT:PSS that provides the Faradaic activity (Note S2, ESI†) does not absorb light since its absorption spectrum has no overlap with the spectrum of the used light source (Fig. S4, ESI†). The temperature of the supercapacitor without solar illumination (in the dark) is ~25 °C (the environment temperature). Fig. 3a and b show the cyclic voltammetry (CV) curves of the supercapacitor with a 0.7 V potential range at scan rates from 5 to 100 mV s^{-1} in the dark and under 1 solar illumination. It can be seen that the CV curves under solar illumination have similar rectangular-like shapes to those in the dark but with higher currents, indicating no new types of reactions and higher amounts of exchanged charges under solar illumination. The CV curves at a scan rate of 5 mV s^{-1} shown in Fig. 3c evidently show the larger CV curve area under solar illumination, indicating a larger specific capacitance. The galvanostatic charge/discharge (GCD) measurements conducted at current densities ranging from 3.3 to 21.1 mA cm^{-3} are shown in Fig. 3d and e. The GCD curves in the dark and under solar illumination have similar triangle shapes. The charging and discharging time both increase, while the IR drop decreases under solar illumination (for example, at a current density of 3.3 mA cm^{-3}, the total charge/discharge time increases from ~224.9 to ~366.5 s and the IR drop decreases from 4×10^{-3} to 2.59×10^{-3} V under 1 solar illumination) (Fig. 3f and Fig. S5a, ESI†), corresponding to an increased capacitance and decreased internal resistance under solar illumination. The calculated volumetric specific capacitances at different CV scan rates and GCD current densities in the dark and under 1 solar illumination are shown in Fig. 3g and h, respectively (calculation processes are shown in Note S3, ESI†). It can be clearly seen that the

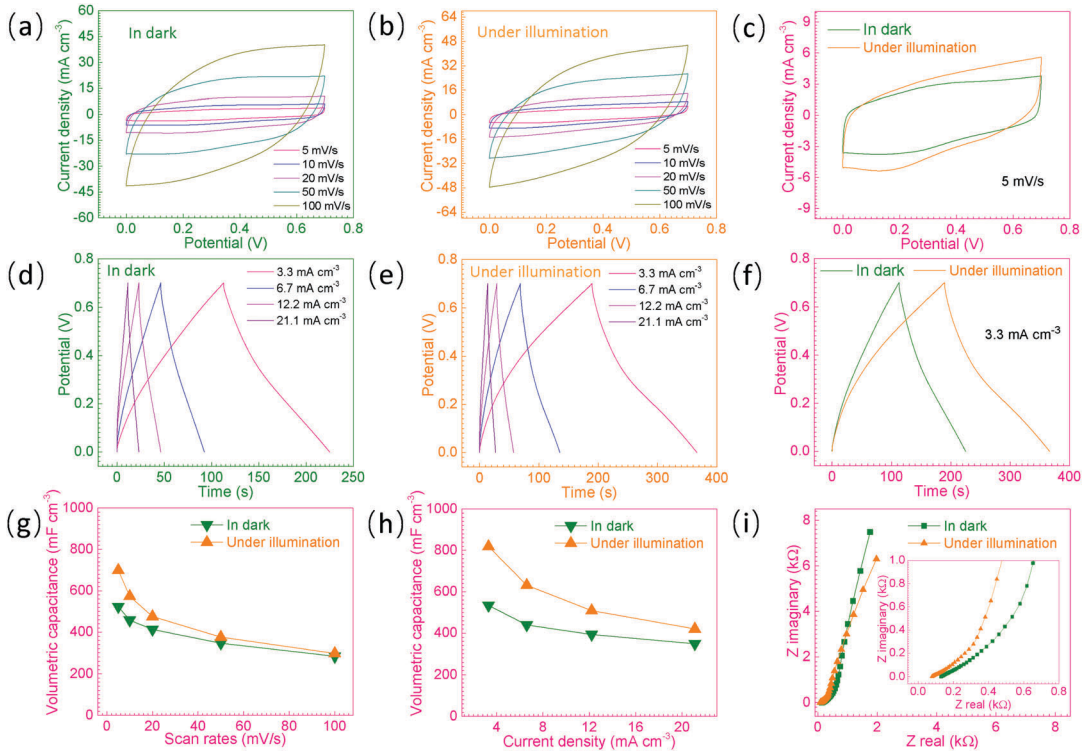

Fig. 3 Electrochemical properties of the supercapacitor in the dark and under 1 solar illumination. (a and b) Cyclic voltammetry (CV) curves at various scan rates for the supercapacitor (a) in the dark and (b) under 1 solar illumination. (c) Comparative CV curves at 5 mV s^{-1} of the supercapacitor in the dark and under 1 solar illumination. (d and e) Galvanostatic charge/discharge (GCD) curves at various current densities for the supercapacitor (d) in the dark and (e) under 1 solar illumination. (f) Comparative GCD curves at 3.3 mA cm^{-3} of the supercapacitor in the dark and under 1 solar illumination. (g and h) Volumetric specific capacitances calculated from the (g) CV curves and (h) GCD curves. (i) Nyquist plots of the supercapacitor in the dark and under 1 solar illumination.

specific capacitance of the supercapacitor increases under solar illumination. In the dark, the volumetric specific capacitances at scan rates from 5 to 100 mV s^{-1} are ~523.5 to ~283.4 mF cm^{-3}, and at GCD current densities from 3.3 to 21.1 mA cm^{-3} are ~534.0 to ~348.3 mF cm^{-3}; under solar illumination, the corresponding values are from ~699.3 to ~297.2 mF cm^{-3}, and from ~818.8 to ~420.4 mF cm^{-3}, respectively.

The electrochemical impedance spectroscopy (EIS) measurements were conducted under open-circuit conditions in the frequency range from ~10^5 to 0.01 Hz, and are shown as Nyquist plots in Fig. 3i. The interception with the real axis is the equivalent series resistance (R_{esr}) including the resistances of the electrolyte and electrodes, which reduces (from ~128 to ~93 Ω) under 1 solar illumination. Note that the R_{esr} obtained from the EIS curves and the internal resistances obtained from the IR drops (Fig. S5b, ESI†) are slightly different, which may be attributed to the system errors of different measurements. The inclined line with a slope of 45° corresponds to the Warburg impedance, which represents the diffusion of ions within the porous electrodes. The projected length of the Warburg-type line on the real impedance axis is equal to one third of the ionic resistance,[37,48] and the ionic resistance decreases (from ~777 to ~369 Ω) under 1 solar illumination, suggesting a lower barrier to ionic transport. The straight line close to vertical at the low-frequency region characterizes the capacitive behavior of the supercapacitor; and the closer to vertical the line is, the closer the supercapacitor behaves as an ideal capacitor. The nearly vertical line at the low-frequency region in the dark indicates the good capacitive behavior of the supercapacitor. The slight shift toward a lower slope under solar illumination suggests an increased deviation from ideal capacitive behavior, which may be due to the increased leakage current induced by the faster self-discharge rate at the elevated temperature.[49,50] The supercapacitor exhibits excellent cycling stability in the dark, with ~99.76% capacitance retained after 16 000 continuous cycles of the GCD test (Fig. S6a, ESI†). The cycling stability declines under 1 solar illumination, with a capacitance retention of ~72.04% after 2000 continuous cycles of the GCD test (Fig. S6b, ESI†), which could be mainly attributed to two reasons. The first reason is the degradation of the solid-state PVA/H_3PO_4 electrolyte that involves the loss of ion exchange groups, intra- or intermolecular dehydration, and decrease in the dielectric constant, which could contribute to decreased capacitance (details in Note S4 and Fig. S7–S9, ESI†). The second reason is that with the increased temperature under solar illumination, there are increased reaction rates of side reactions, which could also contribute to decreased capacitance.[51–54] The coulombic efficiency slightly reduces (from 99.46% to 91.76%) under 1 solar illumination (Fig. S10a, ESI†), which corresponds to the increasing self-discharge rate with increasing temperature under solar illumination.[55] Additionally, the increased reaction rates of the side reactions between the active material and the electrolyte at the increased temperature under solar illumination may also contribute to the decreasing coulombic efficiency.[56–58] The electrochemical property of the supercapacitor shows good repeatability upon periodic dark/illumination cycles (Fig. S11, ESI†), demonstrating that the solar thermal-driven capacitance enhancement is reliable and reproducible.

The relationship between the power density of the solar irradiation and the photothermal temperature of the supercapacitor is shown in Fig. 4a. It can be seen that the temperature increases nearly linearly with the solar power density. The CV curves and the GCD curves have similar shapes at different solar power densities, and the CV curve area and the charge/discharge time both increase with increasing solar power density (Fig. 4b, c and Fig. S12, ESI†), indicating no new types of reactions and an increasing capacitance with increasing solar power density. Fig. 4d and e present the volumetric specific capacitances calculated from the CV curves and GCD curves, respectively, which evidently show the increasing trend of the capacitance with the increasing solar power density. From the EIS curves (Fig. 4f), it can be acquired that the R_{esr} and the ionic resistance both monotonically decrease with increasing solar power density (Fig. S13, ESI†). The energy density $E = C\Delta E^2/2$ and power density $P = \Delta E^2/4R_{esr}$ both have monotonically increasing relationships with increasing solar power density (E increases from ~36.3 to ~55.7 Wh m^{-3} and P increases from ~212.7 to ~349.0 kW m^{-3} when the solar power density increases from 0 to 1 kW m^{-2}, Fig. 4g and h).

A 3D mathematical model has been established to quantitatively understand the mechanism for the solar thermal-driven capacitance enhancement. Note that the details for the modeling and simulation can be found in Note S5 (ESI†). Supposing that no temperature difference exists inside the supercapacitor, the main variable parameters under solar illumination are the temperature T, the conductivities of the electrolyte σ_1 and electrode σ_2, the electric double-layer capacitance C_{dl}, the diffusion coefficient D, and the reaction rate constant k. The σ_1 and σ_2 both increase with the increasing solar power density (Fig. S14, ESI†), and so do the C_{dl}, D and k (details in Note S5, ESI†). The electrochemical performance of the double-layer-type supercapacitor in the dark and under solar illumination is presented in Fig. S15 (ESI†). The C_{dl} increases with the light intensity (Fig. S16b, ESI†), which is mainly due to the electrolyte's increasing dielectric constant with the increasing photothermal temperature (Note S6 and Fig. S17, ESI†). It is found that the D (when changing from 10^{-15} to 10^{-11} m^2 s^{-1}) has nearly no effect on the capacitance (Fig. S18d, ESI†). This may be partially due to the fact that the PEDOT:PSS layer is thin (5 nm) and the effect of diffusion in it is tiny.[59] When the k increases, the capacitance increases at a decreasing rate (Fig. S19, ESI†). A larger reaction rate will induce more ions to participate in the Faradaic reaction; but there exists a maximum reaction ion concentration and the available reaction ions will be limited by the diffusion process when k further increases. Therefore, the increasing rate of the capacitance slows down when k keeps increasing. The simulated GCD curve under 1 solar illumination has a discharging time ~1.7 times longer than that in the dark, which is close to the experimental data (~1.5 times) (Fig. S20a, ESI†). Based on the parameters in the dark, by only changing an individual variable and the T to those under 1 solar illumination each time, it can be obtained that the increases in

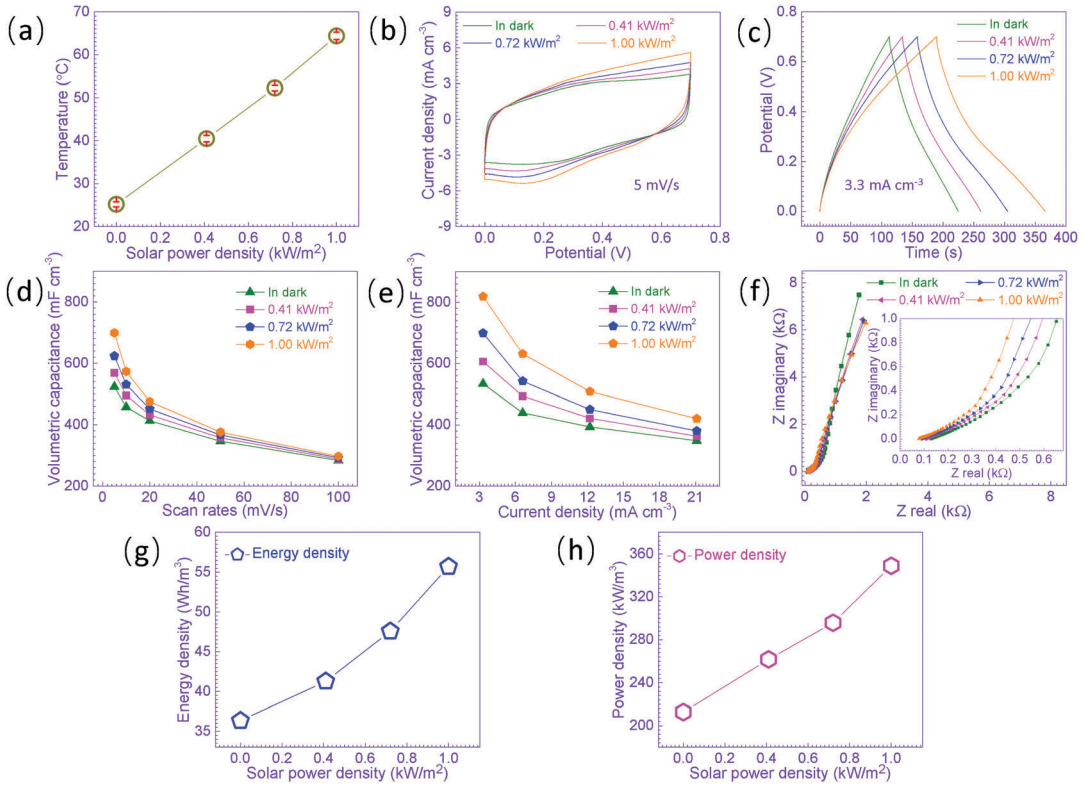

Fig. 4 Electrochemical properties of the supercapacitor under solar illumination at different power densities. (a) Relationship between the photothermal temperature and solar power density. (b and c) The (b) CV curves at 5 mV s^{-1} and (c) GCD curves at 3.3 mA cm^{-3} of the supercapacitor under different light illumination intensities. (d and e) Volumetric specific capacitances of the supercapacitor under different light intensities calculated from the (d) CV curves and (e) GCD curves. (f) Nyquist plots of the supercapacitor under different light intensities. (g) Increasing energy density with the increasing solar power density. (h) Increasing power density with the increasing solar power density.

the σ, C_{dl}, and k all contribute to the higher capacitance (Fig. S20b, ESI†). The increase in the σ leads to a lower internal resistance and a smaller IR drop, thus improving the capacitance. The increase in C_{dl} means an increase in the electric double-layer capacitance component. The increase in k helps to increase the Faradaic capacitance component. The simulated GCD curves also show an increasing discharging time with the increasing solar power density (Fig. S20a, ESI†), which agrees with the experimental results. It should be noted that the real electrochemical processes are more complicated than those in the simulation model, and the parameters are interrelated and impact one another. Hence, for different electrochemical systems, the contribution of each variable parameter to the capacitance variation by the photothermal effect may be different and should be analyzed on a case-by-case basis.

To further verify that the enhanced capacitance under solar illumination is triggered by the photothermal effect. The electrochemical properties of the supercapacitor heated at different temperatures were investigated. The CV, GCD and EIS curves are found to be similar to those at the corresponding photothermal temperatures under solar illumination (Fig. 5a–c), and the cycling stability heated at 63 °C (~70% capacitance retention after 2000 continuous cycles of the GCD test) is lower than that at room temperature (Fig. S21 and S6a, ESI†). It is noticed that the increment of the capacitance (Fig. 5d and e), as well as the decrements of the R_{esr} (Fig. S13a, ESI†), ionic resistance (Fig. S13b, ESI†) and columbic efficiency (Fig. S10b, ESI†) at a heating temperature are all slightly larger than those at the corresponding photothermal temperature. This may be owing to the fact that the average temperature of the whole supercapacitor under solar illumination is actually lower. Firstly, the photothermal temperature recorded by the infrared camera is the surface temperature, and the bottom temperature can be lower. To illustrate this, a simplified model is established to simulate the temperature distribution when under solar illumination (details in Note S7, ESI†). It is found that the main components of the supercapacitor, which are the solid-state PVA/H_3PO_4 electrolyte and 3D-h graphene, both present temperature declines towards the supercapacitor's bottom surface; and the temperature differences between the top and bottom surface both increase with the increasing temperature (Fig. S22b–g, ESI†). Note that the temperature difference along 3D-h graphene is much lower than that along the electrolyte because of 3D-h graphene's much higher thermal conductivity (Table S7, ESI†). Therefore the temperature difference inside the supercapacitor should be mainly determined by the electrolyte. Secondly, there is a temperature transition zone at the supercapacitor boundary when under solar illumination (Fig. 2e), which connects the surrounding temperature with the equilibrium photothermal temperature. Therefore, a temperature decline also exits at the

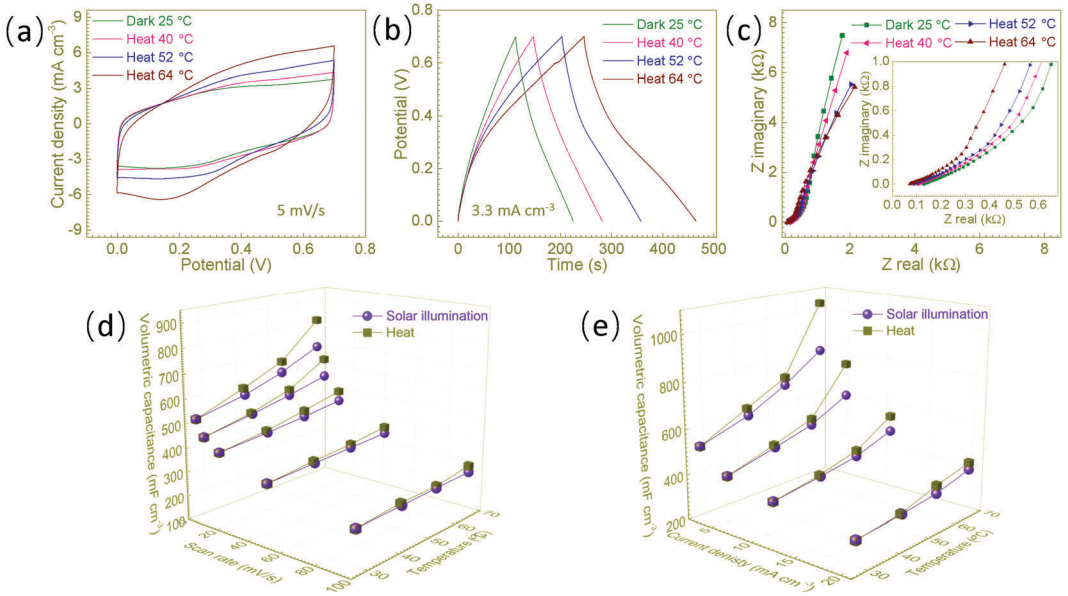

Fig. 5 Electrochemical properties of the supercapacitor heated at different temperatures. (a–c) The (a) CV curves at 5 mV s^{-1}, (b) GCD curves at 3.3 mA cm^{-3} and (c) Nyquist plots of the supercapacitor at different heating temperatures. (d and e) Comparison of the volumetric specific capacitances when heated and under solar illumination calculated from the (d) CV curves and (e) GCD curves.

boundary of the lateral sides when the supercapacitor is under solar illumination.

Conclusions

In summary, the capacitance, energy density and power density of the supercapacitors are all largely enhanced under solar illumination due to the photothermal effect. The supercapacitors use 3D-h graphene that has high broadband light absorption and high thermal conductivity as the electrodes. The supercapacitor has a light absorption of >92.88% in the full solar spectrum, and a surface temperature change (ΔT) of ~39 °C under 1 solar illumination. Compared with without illumination, the capacitance, energy density and power density of the pseudo-type supercapacitor increase by ~1.5 times, ~1.5 times and ~1.6 times under 1 solar illumination, respectively. The capacitance of the double-layer-type supercapacitor increases by ~3.7 times under 1 solar illumination. The mechanism is systematically analyzed and discussed, which agrees with the experimental results. The electrochemical performance of the supercapacitor heated at different temperatures verifies the proposed mechanism. The strategy developed in this work is applicable to supercapacitors based on materials with high solar thermal conversion efficiency, such as carbon materials and nanostructured metals (*e.g.*, Au and Al). It may also be applied to other kinds of energy storage devices such as batteries. Future research could involve further increasing the solar thermal conversion efficiency, shortening the response time, improving the electrochemical cycling stability, and more precisely manipulating the electrochemical performance by light illumination. To further increase the solar thermal conversion efficiency, it is favored that the device material components have high solar thermal conversion efficiencies and the device has an optimized architecture to maximize light absorption; to further shorten the response time, it is preferred that the device material components have low specific heat capacities; to further improve the electrochemical cycling stability, it is necessary to employ an electrolyte that has stable properties over a wide temperature range and further purify the device material components, including the electrolyte, electrode and active material, to remove impurity reagents so as to reduce side reactions; to more precisely manipulate the electrochemical performance, it is feasible to tune the light power density by adding an optical concentrator or attenuator between the light source and the device. In addition, device material components with high thermal conductivities can help make the device temperature uniform; and coating or encapsulating with thermal insulation materials would not only help to make the device temperature uniform but also reduce the dissipation of solar thermal energy, which may face a compromise with light absorption though. Moreover, developing ignition, optical or temperature sensors based on this phenomenon may also represent a potential direction for future work. Overall, this work opens up new frontiers for the application of solar energy and inspires new designs for energy storage devices.

Methods

Synthesis of the 3D-h graphene

(1) A piece of commercial Ni foam (5.5 × 9 × 0.16 cm) was ultrasonically cleaned with ethanol for 10 min, and distilled water for 10 min, and then dried at 65 °C in air. (2) The dried Ni foam substrate was placed in the center of a furnace, the plasma generator of which was made up of Cu coil and radio frequency power (RFG-500 RF Power, Tailong Electronics).

(3) The furnace system was first evacuated to a base pressure of 0.1 Pa and then heated to 700 °C. (4) The temperature was maintained under 100 sccm hydrogen for 10 ~ 30 min to remove residual organic matter and reduce the surface nickel oxide. (5) A methane flow of 7 sccm was introduced into the system with a pressure of 15 Pa, and the plasma generator was turned on with a power of 150 W to generate methane plasma. (6) After depositing for 0.17–3 h, the furnace was cooled to room temperature. (7) The as-synthesized graphene–nickel foam was taken out of the furnace and then placed into a 1 M $FeCl_3$ solution at room temperature overnight or 50 °C for two hours to remove the nickel template. (8) After the etching of the nickel substrate, the 3D-hierarchical (3D-h) graphene foam was cleaned with distilled water and ethanol several times, and then dried in air.

Fabrication of the supercapacitor

(1) Two pieces of the 3D-h graphene foam were cut to the same size. (2) The PEDOT:PSS solution (0.54% in H_2O, purchased from Sigma-Aldrich) was dropped onto the 3D-h graphene foam (~0.25 mL per square centimeter of the graphene foam) and the excess solution was wiped away with filter paper. (3) The wetted 3D-h graphene foams were dried under vacuum at 70 °C for 3 h. (4) The two pieces of the PEDOT:PSS coated 3D-h graphene foam were put onto a clean PET substrate, with a gap between the two. (5) One end of each PEDOT:PSS coated 3D-h graphene foam was connected to a wire by silver paste and the other end was fixed by an epoxy adhesive. (6) The device part constructed in Step 5 was put into a cuboid mold that has a height slightly higher than the 3D-h graphene foam. (7) The liquid-state PVA/H_3PO_4 electrolyte was prepared: 6 g of H_3PO_4 and 6 g of PVA powder (Alfa, 86–89% hydrolyzed, low molecular weight) were added into 60 mL of distilled water, and then the mixture was stirred and heated to 90 °C until the solution became clear. (8) The liquid-state PVA/H_3PO_4 electrolyte was poured into the cuboid mold in Step 6, and the liquid-state electrolyte was dried at 54–60 °C for ~8 h until the solid-state electrolyte filled up the porous electrode. (9) The supercapacitor was obtained by peeling off the PET substrate.

Characterization and measurements

The SEM characterization was carried out using a Hitachi S-4800 scanning electron microscope with an acceleration voltage of 5–30 kV. The Raman spectra were measured using a Jobin Yvon LabRAM HR 800UV spectrometer (514.5 nm laser, 25 mW). The transmittance, reflectance and absorbance spectra were characterized by a UV-vis-NIR Perkin Elmer Lambda 950 spectrophotometer. The dielectric constants of the electrolyte at different temperatures were measured using a SU Series Benchtop Chamber (SU-261) and an Agilent 4294A Precision Impedance Analyzer. The solar light source was provided using a solar simulator produced by Perfect Light FX300. The infrared images of the temperature profiles were recorded using an FLUKE Ti 10 Infrared Camera. The electrochemical performance of the supercapacitor heated at different temperatures was investigated by placing the supercapacitor in an incubator. The electrochemical properties were measured using an electrochemical workstation (Bio-Logic Science VMP3).

Author contributions

F. Y. and F. L. conceived the idea. F. Y., H. R., K. W., K. L., M. T. and M. Z. did the experiments. F. Y., F. L., D. W., H. R., K. D., and X. W. analyzed the data. F. Y., D. W., and F. L. wrote the paper. K. D. and F. Y. did the modeling and simulation for the supercapacitors. Y. H. and F. Y. did the modeling and simulation for the temperature distribution. B. G. did the simulation of the electric field distribution of the graphene. All the authors discussed the results and commented on the manuscript.

Conflicts of interest

There are no conflicts to declare.

Acknowledgements

This work was supported by the National Postdoctoral Program for Innovative Talents of China (BX201600001), the National Key Research and Development Program of China (2016YFA0200103), the National Natural Science Foundation of China (51520105003, 51432002, 51290272 and 51362029), the Ministry of Science and Technology of China (2014CB932500), and the Beijing Municipal Science and Technology Commission (Z161100002116021).

Notes and references

1 N. Armaroli and V. Balzani, *Angew. Chem., Int. Ed.*, 2007, **46**, 52–66.
2 H. Ghasemi, G. Ni, A. M. Marconnet, J. Loomis, S. Yerci, N. Miljkovic and G. Chen, *Nat. Commun.*, 2014, **5**, 4449.
3 L. Zhang, B. Tang, J. Wu, R. Li and P. Wang, *Adv. Mater.*, 2015, **27**, 4889–4894.
4 L. Zhou, Y. Tan, J. Wang, W. Xu, Y. Yuan, W. Cai, S. Zhu and J. Zhu, *Nat. Photonics*, 2016, **10**, 393–398.
5 A. Politano, P. Argurio, G. Di Profio, V. Sanna, A. Cupolillo, S. Chakraborty, H. A. Arafat and E. Curcio, *Adv. Mater.*, 2017, **29**, 1603504.
6 J. Wang, Y. Li, L. Deng, N. Wei, Y. Weng, S. Dong, D. Qi, J. Qiu, X. Chen and T. Wu, *Adv. Mater.*, 2017, **29**, 1603730.
7 P. Yang, K. Liu, Q. Chen, J. Li, J. Duan, G. Xue, Z. Xu, W. Xie and J. Zhou, *Energy Environ. Sci.*, 2017, **10**, 1923–1927.
8 M. A. Shannon, P. W. Bohn, M. Elimelech, J. G. Georgiadis, B. J. Marinas and A. M. Mayes, *Nature*, 2008, **452**, 301–310.
9 G. Ni, G. Li, S. V. Boriskina, H. Li, W. Yang, T. Zhang and G. Chen, *Nat. Energy*, 2016, **1**, 16126.
10 L. Zhou, Y. Tan, D. Ji, B. Zhu, P. Zhang, J. Xu, Q. Gan, Z. Yu and J. Zhu, *Sci. Adv.*, 2016, **2**, e1501227.
11 A. Sutton, T. Shirman, J. V. I. Timonen, G. T. England, P. Kim, M. Kolle, T. Ferrante, L. D. Zarzar, E. Strong and J. Aizenberg, *Nat. Commun.*, 2017, **8**, 14700.
12 Y. Sun, Q. Wu and G. Shi, *Energy Environ. Sci.*, 2011, **4**, 1113–1132.

13 Y. Zhu, S. Murali, M. D. Stoller, K. J. Ganesh, W. Cai, P. J. Ferreira, A. Pirkle, R. M. Wallace, K. A. Cychosz, M. Thommes, D. Su, E. A. Stach and R. S. Ruoff, *Science*, 2011, **332**, 1537–1541.
14 F. Zhang, T. Zhang, X. Yang, L. Zhang, K. Leng, Y. Huang and Y. Chen, *Energy Environ. Sci.*, 2013, **6**, 1623–1632.
15 L. Kou, T. Huang, B. Zheng, Y. Han, X. Zhao, K. Gopalsamy, H. Sun and C. Gao, *Nat. Commun.*, 2014, **5**, 3754.
16 X. Wang, Y. Yin, X. Li and Z. You, *J. Power Sources*, 2014, **252**, 64–72.
17 D. Yu, K. Goh, H. Wang, L. Wei, W. Jiang, Q. Zhang, L. Dai and Y. Chen, *Nat. Nanotechnol.*, 2014, **9**, 555–562.
18 T. Lin, I. W. Chen, F. Liu, C. Yang, H. Bi, F. Xu and F. Huang, *Science*, 2015, **350**, 1508.
19 X. Xiong, D. Ding, D. Chen, G. Waller, Y. Bu, Z. Wang and M. Liu, *Nano Energy*, 2015, **11**, 154–161.
20 K.-H. Choi, J. Yoo, C. K. Lee and S.-Y. Lee, *Energy Environ. Sci.*, 2016, **9**, 2812–2821.
21 Y. Yang, Q. Huang, L. Niu, D. Wang, C. Yan, Y. She and Z. Zheng, *Adv. Mater.*, 2017, **29**, 1606679.
22 S. Zheng, Z.-S. Wu, S. Wang, H. Xiao, F. Zhou, C. Sun, X. Bao and H.-M. Cheng, *Energy Storage Materials*, 2017, **6**, 70–97.
23 A. Rufer, D. Hotellier and P. Barrade, *IEEE Trans. Power Delivery*, 2004, **19**, 629–636.
24 M. Conte, *Fuel Cells*, 2010, **10**, 806–818.
25 J. Wang, X. Li, Y. Zi, S. Wang, Z. Li, L. Zheng, F. Yi, S. Li and Z. L. Wang, *Adv. Mater.*, 2015, **27**, 4830–4836.
26 K. Dai, X. Wang, Y. Yin, C. Hao and Z. You, *Sci. Rep.*, 2016, **6**, 38794.
27 F. Yi, J. Wang, X. Wang, S. Niu, S. Li, Q. Liao, Y. Xu, Z. You, Y. Zhang and Z. L. Wang, *ACS Nano*, 2016, **10**, 6519–6525.
28 K. Dai, X. Wang, F. Yi, Y. Yin, C. Jiang, S. Niu, Q. Li and Z. You, *Nano Res.*, 2018, **11**, 1146–1156.
29 D.-K. Lim, A. Barhoumi, R. G. Wylie, G. Reznor, R. S. Langer and D. S. Kohane, *Nano Lett.*, 2013, **13**, 4075–4079.
30 Q. Jiang, L. Tian, K.-K. Liu, S. Tadepalli, R. Raliya, P. Biswas, R. R. Naik and S. Singamaneni, *Adv. Mater.*, 2016, **28**, 9400–9407.
31 G.-Y. Li, X.-H. Wu, W.-N. He, J.-H. Fang and X.-T. Zhang, *Acta Phys.-Chim. Sin.*, 2016, **32**, 2146–2158.
32 J.-X. Liang, Z.-C. Xiao and L.-J. Zhi, *Acta Phys.-Chim. Sin.*, 2016, **32**, 2390–2398.
33 K.-L. Xia, M.-Q. Jian and Y.-Y. Zhang, *Acta Phys.-Chim. Sin.*, 2016, **32**, 2427–2446.
34 Y. Ito, Y. Tanabe, J. Han, T. Fujita, K. Tanigaki and M. Chen, *Adv. Mater.*, 2015, **27**, 4302–4307.
35 X. Hu, W. Xu, L. Zhou, Y. Tan, Y. Wang, S. Zhu and J. Zhu, *Adv. Mater.*, 2017, **29**, 1604031.
36 H. Ren, M. Tang, B. Guan, K. Wang, J. Yang, F. Wang, M. Wang, J. Shan, Z. Chen, D. Wei, H. Peng and Z. Liu, *Adv. Mater.*, 2017, **29**, 1702590.
37 D. J. Guerrero, X. Ren and J. P. Ferraris, *Chem. Mater.*, 1994, **6**, 1437–1443.
38 C. M. Hessel, V. P. Pattani, M. Rasch, M. G. Panthani, B. Koo, J. W. Tunnell and B. A. Korgel, *Nano Lett.*, 2011, **11**, 2560–2566.
39 H. K. Raut, V. A. Ganesh, A. S. Nair and S. Ramakrishna, *Energy Environ. Sci.*, 2011, **4**, 3779–3804.
40 G. A. Snook, P. Kao and A. S. Best, *J. Power Sources*, 2011, **196**, 1–12.
41 S. B. Kulkarni, U. M. Patil, I. Shackery, J. S. Sohn, S. Lee, B. Park and S. Jun, *J. Mater. Chem. A*, 2014, **2**, 4989–4998.
42 H. Li, Y. Tao, X. Zheng, J. Luo, F. Kang, H.-M. Cheng and Q.-H. Yang, *Energy Environ. Sci.*, 2016, **9**, 3135–3142.
43 Z. Li, T. Huang, W. Gao, Z. Xu, D. Chang, C. Zhang and C. Gao, *ACS Nano*, 2017, **11**, 11056–11065.
44 H. Sun, L. Mei, J. Liang, Z. Zhao, C. Lee, H. Fei, M. Ding, J. Lau, M. Li, C. Wang, X. Xu, G. Hao, B. Papandrea, I. Shakir, B. Dunn, Y. Huang and X. Duan, *Science*, 2017, **356**, 599–604.
45 R. R. Nair, P. Blake, A. N. Grigorenko, K. S. Novoselov, T. J. Booth, T. Stauber, N. M. R. Peres and A. K. Geim, *Science*, 2008, **320**, 1308.
46 M. Liu, X. Yin, E. Ulin-Avila, B. Geng, T. Zentgraf, L. Ju, F. Wang and X. Zhang, *Nature*, 2011, **474**, 64.
47 M. Terazima, N. Hirota, S. E. Braslavsky, A. Mandelis, S. E. Bialkowski, G. J. Diebold, R. J. D. Miller, D. Fournier, R. A. Palmer and A. Tam, *Pure Appl. Chem.*, 2004, **76**, 1083–1118.
48 M. Hughes, G. Z. Chen, M. S. P. Shaffer, D. J. Fray and A. H. Windle, *Chem. Mater.*, 2002, **14**, 1610–1613.
49 R. Kötz, M. Hahn and R. Gallay, *J. Power Sources*, 2006, **154**, 550–555.
50 C. Masarapu, H. F. Zeng, K. H. Hung and B. Wei, *ACS Nano*, 2009, **3**, 2199–2206.
51 N.-S. Choi, Z. Chen, S. A. Freunberger, X. Ji, Y.-K. Sun, K. Amine, G. Yushin, L. F. Nazar, J. Cho and P. G. Bruce, *Angew. Chem., Int. Ed.*, 2012, **51**, 9994–10024.
52 C. Li, X. Zhang, K. Wang, X. Sun, G. Liu, J. Li, H. Tian, J. Li and Y. Ma, *Adv. Mater.*, 2017, **29**, 1604690.
53 D. Puthusseri, V. Aravindan, S. Madhavi and S. Ogale, *Energy Environ. Sci.*, 2014, **7**, 728–735.
54 X. Xia, Y. Zhang, D. Chao, Q. Xiong, Z. Fan, X. Tong, J. Tu, H. Zhang and H. J. Fan, *Energy Environ. Sci.*, 2015, **8**, 1559–1568.
55 B. E. Conway, *Electrochemical Supercapacitors: Scientific Fundamentals and Technological Applications*, Plenum Publishers, New York, 1999.
56 Y. He, X. Yu, Y. Wang, H. Li and X. Huang, *Adv. Mater.*, 2011, **23**, 4938–4941.
57 B. Pillay and J. Newman, *J. Electrochem. Soc.*, 1996, **143**, 1806–1814.
58 N. Liu, Z. Lu, J. Zhao, M. T. McDowell, H.-W. Lee, W. Zhao and Y. Cui, *Nat. Nanotechnol.*, 2014, **9**, 187.
59 H. Kim and B. N. Popov, *J. Electrochem. Soc.*, 2003, **150**, A1153–A1160.

